Dependence of surface orientation of erbium oxide on hydrogen behaviors

Wei MAO[a] , Takumi CHIKADA[b], Akihiro SUZUKI[c], Takayuki TERAI[d], Hiroyuki MATSUZAKI[a]

[a]*The University Museum, The University of Tokyo, 7-3-1 Hongo, Bunkyo-ku, Tokyo 113-8656, Japan*
[b]*Deparment of Chemistry, Graduate School of Science, Shizuoka University, 836 Ohya Suruga-ku Shizuoka 422-8529, Japan*
[c]*Nuclear Professional School, School of Engineering, The University of Tokyo, 2-22, Shirakata-shirane, Tokai, Naka, Ibaraki 319-1188, Japan*
[d]*Department of Nuclear Engineering and Management, School of Engineering, The University of Tokyo, 7-3-1 Hongo, Bunkyo-ku, Tokyo 113-8656, Japan*

(Received: 17 September 2014 / Accepted: 19 January 2015)

Erbium oxide is used as tritium permeation barrier in fusion blanket systems, where a hydrogen isotope is adsorbed on the surface, diffusion from the surface, etc. In this article, based on first-principles calculations, we examine the effect of surface orientation on the H behaviors in cubic Er_2O_3 surfaces. It was found that the comparative stability of (110), (111), and (001) surfaces is predicted to be: (111) > (110) > (001). The behaviors of H adsorption and penetration in cubic Er_2O_3 (110) and (111) surfaces are predicted to be somewhat different from those in cubic Er_2O_3 (001) surface. Consequently, we conclude that the surface orientation dependence of the surface properties should be noted in terms of H adsorption and penetration in Er_2O_3 surfaces.

Keywords: Er_2O_3 surfaces, density-functional theory, H adsorption, H penetration

1. Introduction

One of the key components of deuterium (D)-tritium (T) fuelling cycle in fusion blanket systems is the tritium recovery in which tritium permeation barrier (TPB) plays an important role in containing and handling D and T within the reactor building and controlling hydrogen isotope release to the environment without incurring exorbitant costs [1,2]. As to barrier materials, erbium oxide (Er_2O_3) attracts much attention in the application of TPB due to high permeation reduction factor (PRF), good compatibility with liquid lithium, high thermodynamics stability at high temperatures and in air and high electrical resistivity [3-7]. In addition, Er_2O_3 has one of the lowest Gibbs free energy of formation among all binary oxide ceramics [5,6]. As a result, Er_2O_3 has been selected as one of the candidate materials for TPB coatings.

Suppressing H isotope permeation in TPB coatings explains the importance of interaction between atomic hydrogen and erbium oxide [7], and hence much work is required to be devoted to both experimental and theoretical studies of the interaction. In the interaction, it is necessary to understand the thermodynamics and kinetics of hydrogen adsorption on Er_2O_3 surfaces and subsequent hydrogen behavior in bulk Er_2O_3, including penetration, diffusion, and trapping. As recently reported in Refs. [8,9], density functional theory (DFT) calculations have become a valuable tool to elucidate the structures and determine the dynamics of interstitial H in metals, alloys and ceramics, and are used to successfully predict the microscopic behavior of H in oxides such as Cr_2O_3, TiO_2, SiO_2 and Al_2O_3 [10-13]. Therefore, it is essential to apply DFT calculations to the studies on the interaction between atomic hydrogen and Er_2O_3 surfaces.

Interest in the adsorption and penetration of hydrogen atoms in Er_2O_3 surfaces stems mainly from its relevance in TPB coatings. Cubic (001), (110) and (111) surfaces of Er_2O_3 were studied based on the experimental results of X-ray diffraction measurement [7,14]. On the basis that one must understand clean surfaces before one can understand how they interact with their environment, we have placed emphasis on those surfaces regarding to surface structure and electronic properties of Er_2O_3. Subsequently, we discussed H adsorption and penetration in the surfaces via DFT calculations. We provide computational details in Sec. II and then present and discuss our results in Sec. III. Finally, we summarize our work in Sec. IV.

2. Computational details

author's e-mail: mao@nuclear.jp

The computational simulations performed in this study were done using spin-polarized DFT calculations as implemented in the Vienna Ab Initio Simulation Package (VASP) and the Generalized Gradient Approximation (GGA) of Perdew and Wang (PW91) [15] for electron exchange and correlation. The kinetic energy cutoff for the planewave basis set is set to 500.0 eV for all DFT calculations: increasing the cutoff resulted in variations in the total energy of < 2 meV/atom (0.192 kJ· mol^{-1}/atom). The surface and the adsorbate-systems have been simulated using a slab model, which includes 12-16 stoichiometric layers relaxed and unrelaxed and a vacuum region (>1.0 nm). The slabs are tested when increasing one stoichiometric layer results in variations of surface energy less than 0.05 J/m^2. Periodic boundary conditions are used, with the one electron pseudo-orbitals expanded over a plane wave basis set. The *K*-meshes are obtained from Monkhorst-Pack scheme [16].

The sampling of the Brillouin zone is performed using k-meshes of 4×4×1 for (1×1) surface unit cell. For the bulk Er_2O_3 consisting of 32 Er and 48 O atoms, we use a mesh size of 4×4×4 for k-point sampling. These above k-meshes have been tested to be converged to < 1 meV/atom (0.096 kJ· mol^{-1}/atom). Atomic relaxations are performed regarding to a conjugate gradient alogirithm [17] and the force on each atom is converged to be less than 1 meV/nm (0.096 kJ· mol^{-1}/nm). During the optimization both the adsorbate (H) and the Er&O atoms in the top 3-6 stoichiometric layer of the slab are allowed to relax while the remaining Er&O atoms of the slab are frozen at bulk optimized configurations. In addition, dipole corrections originally introduced by Neugebauer and Scheffler [18] are included in order to correct for the errors introduced by the use of periodic boundary conditions. Thus, the adsorption energy (E_{ads}) of adsorbate H considering dipole correction can be calculated as [19]

$$(E_{ads})_d = \left[E(S)_{H\to d} - E(S) - NE(H)\right]/N \qquad (1)$$

where $E(S)_{\to d}$ refers to the energy of the system when H atom is d distance apart from the Er_2O_3 surface, and $E(S)$ is the energy of the Er_2O_3 surface, and $E(H)$ is the energy of ground state isolated H atom/H_2 molecule with spin polarization. H diffusion from the surface to the solute site in the bulk is calculated using climbing image nudged elastic band (CINEB) method [20] as implemented in DFT calculations.

To gain further understanding of the interaction between the H atom and the cubic Er_2O_3 (001) surface, we have presented the charge density plot calculated including the dipole correction. Consideration of quantum effects [21] is important at low temperature for light species such as atomic H. Therefore, zero-point-energy (ZPE) corrections have been considered at the high-symmetry adsorption sites by summing up the zero-point vibrational energies of the H`s normal mode, i.e. $ZPE = 1/2\sum h\nu_i$, where ν_i is the real normal mode frequency [21,22].

3. Results and discussions

3.1. Bulk Er_2O_3

In the unit of cubic Er_2O_3, it belongs to space group Ia3 and has 32 Er atoms occupying the 8a and 24d equipoints and 48 O atoms occupying 48 e equipoints. The lattice constant of 1.0545 nm derived by DFT calculations and fitting with Birch-Murnaghan 3rd-order equation of state (EOS) [23] corresponds well with the experimental data of 1.05431 nm [5]. The corresponding bulk modulus has also been calculated using the above euqtion as Bo = 148.0 GPa, in good agreement with the experimental result Bo = 140.7 GPa [6,24] within a deviation of 5%. The electronic density of states (DOS) of bulk Er2O3 has been calculated using GGA, as shown in Fig. 1. The highest occupied valence band exhibits mainly O 2p features while the lowest unoccupied conduction band mainly consists of Er 5d electrons. This suggests that strong ionic characteristics with weak covalency exist in Er-O bonding in bulk Er_2O_3.

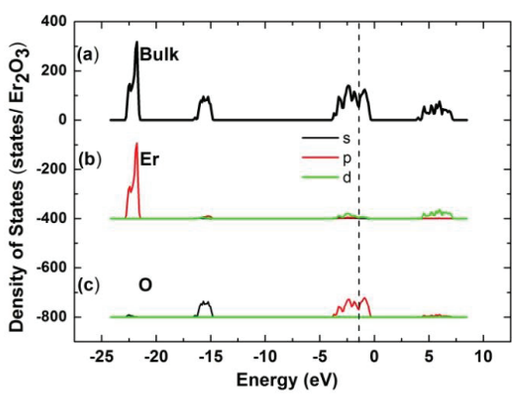

Fig. 1. Total electronic density of states (DOS) of cubic Er_2O_3, (b) partial DOS of Er atoms of cubic Er_2O_3 and (c) partial DOS of O atoms of cubic Er_2O_3. The dash line corresponds to the Fermi energy levels in the Er_2O_3 bulk.

In addition, band structures of Er_2O_3 are calculated at 45 regularly spaced k points in the irreducible portion of Brillouin zone (BZ) by straightforward matrix diagonalization. calculated band structures along the high-symmetry axes of the BZ for Er_2O_3 are shown in Fig. 2. The calculated direct GGA gap of 4.01 eV at Γ is underestimated compared with the experimental data of 5.30 eV [25]. As is well known, this discrepancy stems from the GGA in the density-functional theory. However, the large band gap estimated apparently suggests that Er_2O_3 is a good insulator.

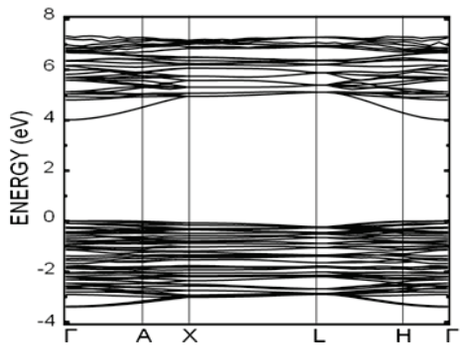

Fig. 2. Calculated band structures of Er_2O_3.

3.2. Surface structural and electronic properties

As reported in Ref. [26], surface energy has become one of the critical parameters determining the stability of surface terminations. To obtain surface energy from DFT calculations, we use a supercell (slab) approach at T = P = 0. For Er_2O_3 surfaces, it can be calculated as

$$\sigma = \left(2E_{\mathrm{tot}}^{\mathrm{slab}} - N_{\mathrm{Er}}E_{\mathrm{tot}}^{\mathrm{bulk}}\right) - (2N_{\mathrm{O}} - 3N_{\mathrm{Er}})\mu_{\mathrm{O}} / 2A \quad (2)$$

where $E_{\mathrm{tot}}^{\mathrm{slab}}$ refers to the total energy of the slab supercell, $E_{\mathrm{tot}}^{\mathrm{bulk}}$ is the energy for bulk Er_2O_3 per formula unit (f.u.), and A is the surface area. N_{Er} and N_{O} represent numbers of Er atoms and O atoms in the slab, respectively. Therefore, the (N_{O}−1.5N_{Er}) are excessive oxygen beyond stoichiometric Er_2O_3 units in the slab. μ_{O} is the chemical potential of oxygen and defined as the variation of the O chemical field between one O_2 molecule and one Er_2O_3 formula unit.

According to Eq. (2), we have calculated surface energy for Er_2O_3 (110) and (111) surfaces with different surface terminations, as shown in Fig. 3. After relaxation, the surface energies of 3.04×10^{-3} kJ/m^2 and 6.01×10^{-3} kJ/m^2 are derived for stoichiometric Er_2O_3 (111) and (110) surfaces respectively, somewhat lower than the value of 9.19×10^{-3} kJ/m^2 for stoichiometric Er_2O_3 (001) surface. Other non-stoichiometric surfaces, such as (110)-O rich, (111)-O rich, and (111)-Er rich surfaces, are unstable due to variations of surface energies depending on the chemical potential/field of oxygen atoms. Consequently, it is considered that the stability of low-index cubic (001) and (110) surfaces mainly depends on the ratio of Er:O at room temperature, in good agreement with that of Er_2O_3 (001) surface [19]. In other words, the stoichiometric (111), (001), and (110) surfaces are the most stable surfaces because surface energy is independence of the chemical field of oxygen at room temperature. This basically corresponds to the results of XRD examinations that the (111), (001), and (110) orientations are found in the same coatings of Er_2O_3 [3,14,27,28]. In addition, the density of states (DOS) of stoichiometric Er_2O_3 (110) and (111) surfaces are presented in Fig. 4. It was found that band gaps between conduction bands and valence bands are small in both Er_2O_3 (110) and (111) surfaces. The two surfaces are predicted to be some metallic character, similar to that of Er_2O_3 (001) surface [19].

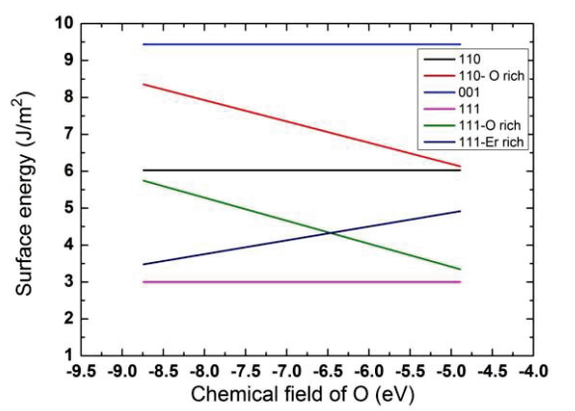

Fig. 3. Surface energies for various surfaces of cubic Er_2O_3 versus chemical potential of oxygen. (001) surface is terminated by single Er atom layer while (111) and (110) surfaces are terminated by a mixed layer with Er and O atoms. (110)-O rich and (111)-O rich surfaces are terminated by single Er atom layer while (111)-Er rich surface is terminated by single O atom layer.

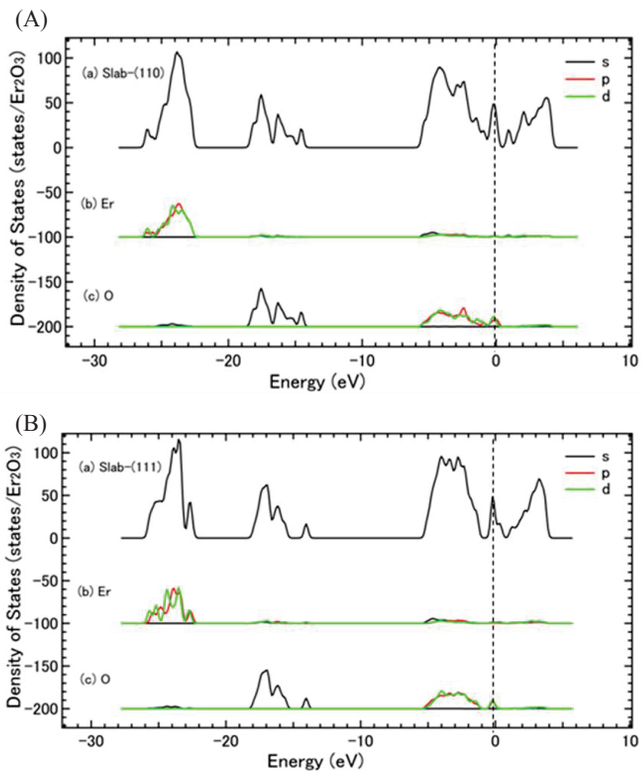

Fig. 4. (A) Density of states (DOS) of the isolated cubic Er_2O_3 (110) surface slab, and (B) DOS of the isolated cubic Er_2O_3 (111) surface slab: (a) DOS of the isolated cubic Er_2O_3 (110) and (111) surfaces, (b) partial DOS of Er atoms of the isolated cubic Er_2O_3 (110) and (111) surfaces, and (c) partial DOS of O atoms of the isolated cubic Er_2O_3 (110) and (111) surfaces. The Fermi energy levels are represented as the vertical dash line in each diagram.

3.3. Hydrogen adsorption on Er_2O_3 surfaces

After analyzing surface structural and electronic properties of stoichiometric Er_2O_3 (110) and (111) surfaces, we studied several possibly high-symmetry sites on those surfaces for H adsorption. These sites are on top of Er atom, Er-Er bridge, Er-O bridge, O atom, and fourfold hollow position surrounded by four neighbouring O atoms. It was found that the fourfold hollow position is the most stable adsorption site due to the largest adsorption energy. More emphasis is therefore placed on the most stable adsorption site (e.g. A position). H adsorption energies at the A site on the (110) and (111) surfaces were calculated using Eq.(2), as shown in Table 1. It was found that adsorption energies on the most stable site (A) of Er_2O_3 (110) and (111) surfaces are -2.01 eV/H (-1.92 eV/H with ZPE corrections) and -2.67 eV/H (-2.56 eV/H with ZPE corrections), somewhat lower than that (-3.12 eV (-2.99 eV/H with ZPE corrections)) on Er_2O_3 (001) surface [19].

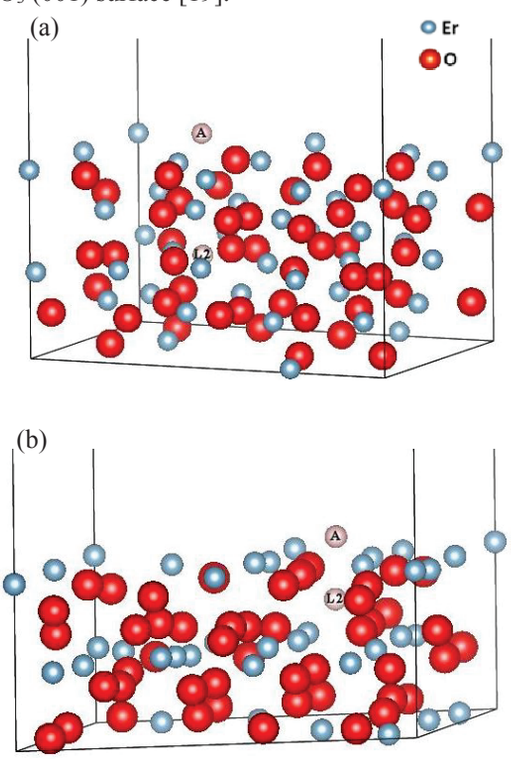

Fig. 5. Stable adsorption site (A) and solution site (L2) for H adsorption and penetration on (a) cubic Er_2O_3 (110) surface and (b) cubic Er_2O_3 (111) surface.

Table 1 Hydrogen adsorption energy in the stable adsorption site (A) on Er_2O_3 (110) and (111) surfaces. The hydrogen adsorption energy on Er_2O_3 (001) surface is attached in comparison with those on Er_2O_3 (110) and (111) surfaces. Values in parentheses are ZPE corrected.

Surface	Adsorption energy (eV/H)
(110)	-2.67 (-2.56)
(111)	-2.01 (-1.92)
(001)	-3.12 (-2.99)

The large adsorption energies verify the strong covalent of H-O bonds and weak H-Er interactions. This is also confirmed by the results of LDOS (in Fig. 6) and charge density (in Fig. 7) of Er_2O_3 (110) and (111) surfaces in comparison with those of Er_2O_3 (001) surface [19], in which metallic character of H-Er interactions is very weak due to negligible variations of conduction bands and Er charge densities, as indicated in Fig. 6 and Fig. 7. Consequently, H adsorption on Er_2O_3 (110) and (111) surfaces are not a physisorption but chemisorption at the expense of the formation of H-O covalent bonds. Although the mechanism of H adsorption on Er_2O_3 (110) and (111) surfaces is the same as that on Er_2O_3 (001) surface, the large deviations of adsorption energy among them results in the dependence of surface orientation and H adsorption.

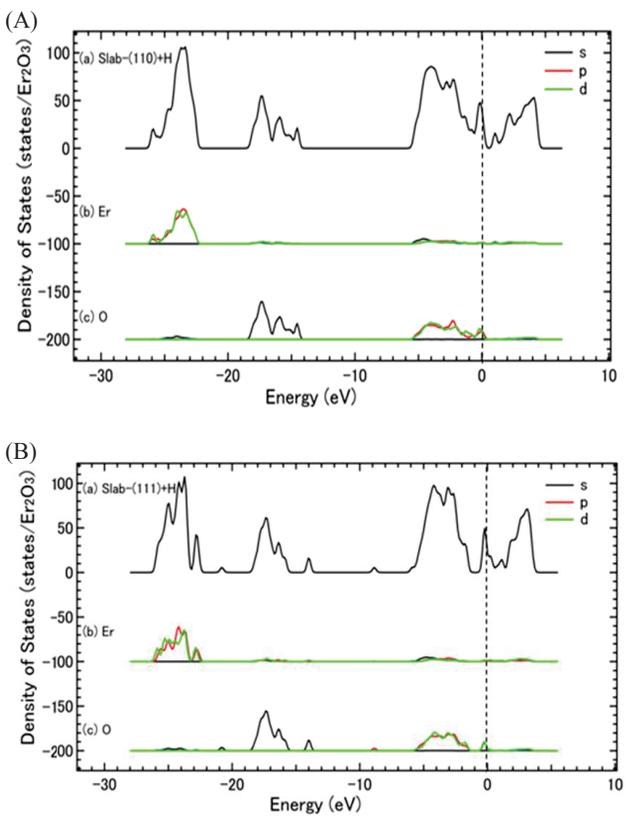

Fig. 6. Total density of states (DOS) of (A) the isolated cubic Er_2O_3 (110) and (B) the isolated cubic Er_2O_3 (111) surface slabs after H adsorption. Partial DOS of Er atoms and O atoms of the two isolated cubic surface slabs after H adsorption are indicated along with DOS using the small Fig. (a), Fig. (b), and Fig. (c) respectively. The Fermi energy levels are represented as the vertical dash line in each diagram.

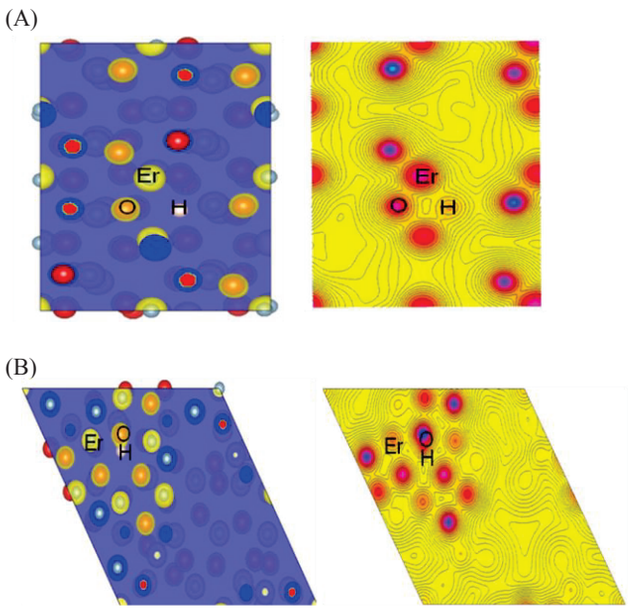

Fig. 7. Charge densities of (A) cubic Er_2O_3 (110) surface and (B) cubic Er_2O_3 (111) surface after H adsorption. H atom strongly bonds with O atoms while it weakly interacts with Er atoms by electron transfer.

3.4. Hydrogen penetration from Er_2O_3 surfaces

After analyzing H adsorption on Er_2O_3 (110) and (111) surfaces, we also studied the process of H penetration from those surfaces, using the models in Fig. 5. A site is determined as the most stable adsorption position. Figure 5 shows a possible high-symmetry solution site (bulk site), L2, located at tetrahedral site (TS). As TS position is energetically favorable for H penetration, we studied H penetration in terms of penetration energies and penetration pathways from A to L2 site. With CINEB method, the penetration energies of 1.6 eV (1.58 eV with ZPE corrections) and 2.4 eV (2.36 eV with ZPE corrections) are defined for cubic Er_2O_3 (110) and (111) surfaces respectively, as shown in Fig. 8. The penetration energy from the (110) surface is close to that from the (001) surface [29], but somewhat lower than that from the (111) surface. Therefore, it is considered that the behavior of H penetration depends on surface orientations of cubic Er_2O_3.

3.5. Quantum effects on H behaviors in Er_2O_3 surfaces

Quantum effects on H behaviors in Er_2O_3 were considered in terms of zero-point energy (ZPE) corrections and H isotope effect. Considering an isotope effect of hydrogen, we substituted deuterium/tritium for hydrogen to simulate its behaviors in Er_2O_3 surface via DFT calculations. The pseudopotential for H, D and T is different due to their distinguished mass (m_H:m_D:m_T =1:2:3), in which the pseudopotential of D/T is constructed by substituting D/T mass for hydrogen mass in the H pseudopotential. The total potential energies were therefore calculated for H, D and T, respectively. From the DFT calculations, we found that the difference of total potential energies, at the critical sites between interstitial H, D and T atoms was less than 10^{-4} eV in terms of perfect and imperfect Er_2O_3. Although H, D and T atoms possess different normal mode frequencies [22],

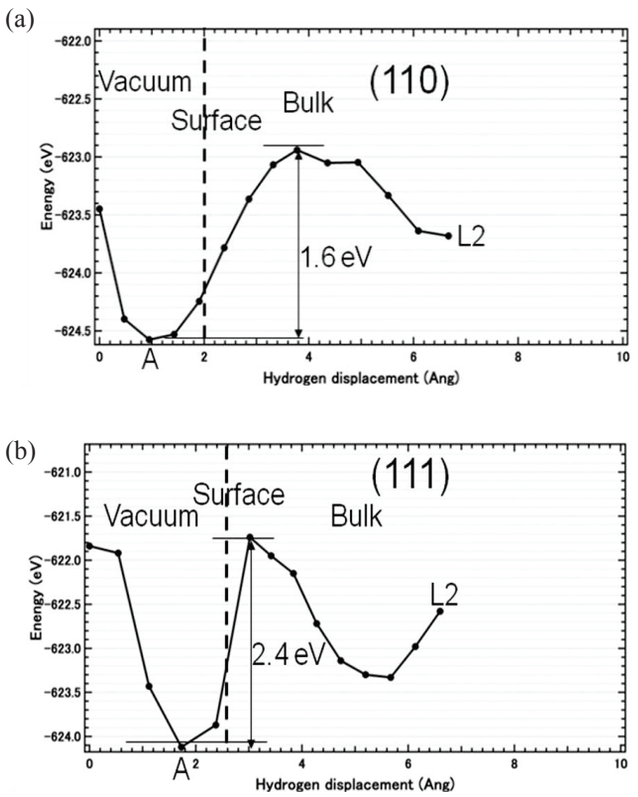

Fig. 8. Energy profile for H adsorption and penetration on (a) Er_2O_3 (110) surface with a penetration energy of 1.6 eV, and (b) Er_2O_3 (111) surface with a penetration energy of 2.4 eV. The penetration energies are calculated by CINEB using 12 images, and ZPE corrections are not included in the profile of potential energies.

ZPE corrections of H/D/T adsorption energies, penetration and diffusion energy barriers verify the same fact that the deviation of the energies is less than 0.05 eV between H, D and T atoms. Consequently, it is considered that the isotope effect would be ignored within 0.05 eV. This neglect approach is reasonable because H/D/T atom is much lighter than the oxygen and erbium atoms.

4. Conclusions

The main findings of this study can be summarized as follows:

1) The native structural and electronic properties of cubic Er_2O_3 surfaces are studied. It was found that both surface energies and electronic structures of the

surface mainly depend on the ratio of Er:O.

2) Considering quantum effects, H behaviors (e.g. adsorption, penetration) in cubic Er_2O_3 surfaces are investigated in terms of density of states, adsorption energy, penetration energy, etc.
3) From the comparisons of surface properties of (110), (111), and (001) surfaces of cubic Er_2O_3, it is considered that the effect of surface orientations on surface properties should be noted in terms of H adsorption energy and penetration energy. The comparative ability of H adsorption on Er_2O_3 surfaces is predicted to be: (111) < (110) < (001). In addition, H penetration from (111) surface is predicted to be much more difficult than that from (110) and (001) surfaces.

As H adsorption and penetration play an important role in the surface effects of erbium oxide, the dependence of surface orientation on H behaviors will provide a fundamental understanding of the microscopic behaviors of H on the basal plane of erbia in the process of H permeation.

Acknowledgments

This work was supported in part by GoNERI, the Global Center of Excellence (G-COE) Program of the Nuclear Education and Research Initiative of the Japan Society for the Promotion of Sciences (JSPS).

References

[1] V.A. Maroni, Tritium Processing and Containment Technology for Fusion Reactors: Perspective and status, Proc. Second Topical Meeting on the Technology of Controlled Nuclear Fusion, USERDA Report CONF-760935-P3 (1976) P. 799.
[2] F. N. Flakus, At. Energy Rev.**13**, 587 (1975).
[3] D. Levchuk, S. Levchuk, H. maier, H. Bolt, A. Suzuki, J. Nucl. Mater. **367-370**, 1033 (2007) 1033.
[4] Z. Yao, A. Suzuki, T. Muroga, K. Katahira, J. Nucl. Mater. **329-333** , 1414 (2004).
[5] Y.E. Bogatov, A.K. Molodkin, M.G. Safronenko, Y.Y. Nevyadomskaya, Russ. J. Inorg. Chem. **39**, 211 (1994).
[6] L. Eyring, The binary rare earth oxides, in: Handbook on the Physics and Chemistry of Rare Earths, vol. 3. K.A. Gschneider Jr., L. Eyring, (eds), North Holland Publishing Co., Amsterdam, Netherlands, 1979, pp. 337-98.
[7] T. Chikada, A. Suzuki, C. Adelhelm, T. Terai, T. Muroga, Nucl. Fusion **51**, 063023 (2011).
[8] K. Honkala, A. Hellman, I.N. Remedeiakis, Á. Logadóttir, A. Carlsson, S. Dahl, C.H.Christensen, J.K. Nørskov, Science **507**, 555 (2005).
[9] D.S. Sholl, Journal of Alloys and Compounds **446–447**, 462 (2007).
[10] C.F. Chen, H.B. Yu, S.Q. Zheng, Science China Technological Sciences **54**, 88 (2010).
[11] S.C. Li, Z.R. Zhang, D. Sheppard, B.D. kay, J.M. White, Y.G. Du, I. Lyubinetsky, G.Henkelman, Z. Dohnalek, Journal of the American Chemical Society **130**, 28 (2008).
[12] B. Tuttle, Physical Review B **61**, 4417 (2000).
[13] A.B. Belonoshko, A. Rosengren, Q. Dong, G. Hultquist, C. Leygraf, Physical Review B **69**, 024302 (2004).
[14] T. Chikada, A. Suzuki, T. Kobayashi, H. Maier, T. Muroga, J. Nucl. Mater. **417**, 1241 (2011) .
[15] G. Kresse, J. Furthmuller, Phys. Rev. B **54**, 11169 (1996).
[16] H.J. Monkhorst, J.D. Pack, Phys. Rev. B **13**, 5188 (1976).
[17] B. Hinnemann, E.A. Carter, J. Phys. Chem. **111**, 7105 (2007).
[18] J. Neugebauer, M. Scheffler, Phys. Rev. B **46**, 16067 (1992) .
[19] W. Mao, T. Chikada, K. Shimura, A. Suzuki, K. Yamaguchi, T. Terai, J. Nucl. Mater. **443**, 255 (2013).
[20] H. Jónsson, G. Mills, K. W. Jacobsen, Classical and Quantum Dynamics in Condensed Phase Simulations, edited by B. J. Berne, G. Ciccotti and D. F. Coker (World Scientific, Singapore, 1998), pp. 385-404.
[21] D.E. Jiang, E.A. Cater, Phys. Rev. B **70**, 064102 (2004).
[22] D.F. Johnson, E.A. Cater, J. Mater. Res. 25 (2010) 315.
[23] F. Birch, Phys. Rev. **71**, 809 (1947) .
[24] A.A. Sharif, F. Chu, A. Misra, T.E. Mitchell, J.J. Petrovis, J. Am. Soc. **83**, 2246 (2000).
[25] L.R. morse, P.P. Day, C. Felinto, H. Brito, J. Chem. Thermodynamics **25**, 415 (1993).
[26] C.H. Chen, Z.F. Hou, X.G. Gong, Comput. Mater. Sci. **44**, 46 (2008).
[27] R. Xu, Y.Y. Zhu, S. Chen, F. Xue, Y.L. Fan, X.J. Yang, Z.M. Jiang, J. Crystal Growth **277**, 496 (2005).
[28] Y. Zhu, R. Xu, S. Chen, Z.B. Fang, F. Xue, Y.L. Fan, X.J. Yang, Z.M. Jiang, Thin Solid Films **508**, 86 (2006).
[29] W. Mao, T. Chikada, A. Suzuki, T. Terai Fusion Eng. Des. **89**, 1294 (2014).